Mechanism and thermal effects of phytic acid-assisted porous carbon sheets for high-performance lithium–sulfur batteries†

Riguang Cheng,[a] Jiaxi Liu,[a] Pantrangi Manasa,[b] Mi Zhou,[c] Yanxun Guan,[a] Kexiang Zhang,[a] Xiangcheng Lin,[a] Federico Rosei, [d] Aleskey A. Pimerzin,[e] Hans Jürgen Seifert,[f] Fen Xu, *[a] Lixian Sun, *[a] Dan Cai,*[a] Julan Zeng,[g] Zhong Cao[g] and Hongge Pan[h]

High energy density, stable, and inexpensive electrode materials have the potential to improve the performance of lithium–sulfur (Li–S) batteries. Developing high porosity, high conductivity, and a network framework for multidirectional ion transfer in Li–S batteries, on the other hand, remains a significant challenge. Nitrogen and phosphorus co-doped porous carbon sheets (PCS900) are designed and synthesized here with high porosity and abundant active sites. PCS900 can withstand high sulphur loading while also providing multidirectional ion transport channels. Density functional theory (DFT) calculations indicate that nitrogen and phosphorus co-dopants play an important role in suppressing the shuttle effect *via* the chemical interaction between sulfur and the carbon framework. At a current density of 1 C, the PCS900/S electrode has an initial specific capacity of 737 mA h g^{-1}, and the average capacity decay rate per 500 cycles is as low as 0.079%. Furthermore, the heat released during the discharging process is greater than the heat released during the charging process due to the combination of *in situ* XRD and microcalorimetry techniques.

1. Introduction

Currently dominant lithium-ion batteries (LIBs) are approaching their theoretical capacity limit.[1–3] Lithium–sulfur (Li–S) batteries are being widely studied and are expected to become the next generation of energy storage devices, because their theoretical energy density is as high as 2600 W h kg^{-1},[4] which is nearly four times that of conventional LIBs; they are now the subject of extensive research and are anticipated to become the next generation of energy storage devices. Sulfur is also a plentiful element on Earth, non-toxic, and simple to produce, which makes it very appealing as a cathode material for energy storage devices, smart grids, and electric vehicles.[5,6] However, the insulating qualities of sulfur and lithium sulfide result in slow electrochemical redox kinetics, and the shuttle effect is brought about by the dissolution of intermediate polysulfides[7–9] and causes the loss of active sulfur. These issues, such as low sulfur consumption, short life cycles, and low energy density, severely impede the electrochemical performance of lithium–sulfur batteries and severely restrict their practical application.[10–12]

Research on cathode materials has become essential for the development of high-performance lithium–sulfur batteries since the insulation of sulfur is the primary drawback of lithium–sulfur batteries.[13] The problem of poor sulfur conductivity can be greatly reduced when sulfur with good conductivity is mixed with certain structural matrix. In the meantime, the dissolution of the intermediate product can be successfully prevented by physical or chemical adsorption on the sulfur-

[a]*School of Materials Science & Engineering, Guangxi Key Laboratory of Information Materials and Guangxi Collaborative Innovation Center of Structure and Property for New Energy and Materials, Guilin University of Electronic Technology, Guilin 541004, PR China. E-mail: sunlx@guet.edu.cn, xufen@guet.edu.cn, dancai1985@guet.edu.cn*

[b]*University of electronic Science and Technology of China, Chengdu, 611731, PR China*

[c]*Huaneng Beijing Co-Generation Co., Ltd., Beijing, 100000, PR China*

[d]*Centre Énergie, Matériaux et Télécommunications, Institut National de la Recherche Scientifique, 1650 Boul. Lionel Boulet, Varennes, Québec, J3X1P7, Canada*

[e]*Chemical Department, Samara State Technical University, Samara, 443100, Russia*

[f]*Institute for Applied Materials, Karlsruhe Institute of Technology, Hermann von Helmholtz Platz 1, 76344 Eggenstein Leopoldshafen, Germany*

[g]*Hunan Provincial Key Laboratory of Materials Protection for Electric Power and Transportation, Changsha University of Science & Technology, Changsha 410114, PR China*

[h]*School of New Energy Science and Technology, Xi'an Technological University, China*

carrying material, increasing the cycling stability of the lithium–sulfur batteries. The properties of the sulfur cathode have been enhanced through the design and synthesis of a number of composite materials. Carbon materials, inorganic compounds, and conductive polymers are the three general groups of matrix materials used for lithium–sulfur battery composites.[14,15]

Graphene derivatives are carbon compounds with a single layer made up entirely of carbon atoms and massless Dirac fermions.[16] Graphene derivatives are efficient substrates for supporting sulfur in lithium–sulfur batteries due to their high specific surface area, strong electronic conductivity, mechanical characteristics, and superior chemical and thermal stability. To some extent, sulfur insulation can be avoided by encasing sulfur in graphene sheets to create a two-dimensional graphene/sulfur composite material.[17] Its mechanical strength can inhibit the volume expansion of sulfur and greatly improve the cycling performance. However, because of its single-layer open structure, which limits polysulfide collection and reduces sulfur storage capacity, the material has a limited capacity for coulombic efficiency and cycling stability. In order to create a porous structure[18] with a bigger response space, graphene nanosheets are combined. Inhibiting the reaction and transmission of electrons and ions in three-dimensional space as well as the dissolution of polysulfides in the electrolyte are advantageous. A good method for creating composites as positive electrodes for lithium–sulfur batteries is to use graphene, a potential carrier material for encasing or anchoring sulfur.

In three dimensions, graphene can offer a reliable network for transporting electrons and can adjust to changes in sulfur's volume.[19] However, there are drawbacks to the production of graphene, including a lengthy cycle, high expense, high risk, and unfriendly environmental practices. It merely has a single layer of carbon atoms and a small amount of sulfur. According to the findings of studies on materials related to three-dimensional graphene, one of the most important steps in the design and synthesis of lithium–sulfur battery cathodes is the creation of three-dimensional and diverse tunable structural materials with high conductivity, high specific surface area, and high porosity.

Generally speaking, heteroatoms (N, P, and B)[20–24] can be doped to enhance carbon materials' conductivity and encourage electrochemical reaction during charge and discharge. N-doped porous carbon materials can be prepared in a variety of ways, although the majority of them require pyrolyzing nitrogen-rich carbon compounds (such as melamine, urea, *etc.*).[25,26] The most common methods for achieving phosphorus doping are heating hypophosphite until breakdown, synthesis of organic phosphorus sources, hydrogen reduction of phosphorus source salts, *etc*. Every technique has some drawbacks.[27] For instance, the synthesis process is combustible, the equipment must withstand corrosion to a high degree, and the synthesis uses and generates very toxic gases. Phytic acid, with the chemical formula of $C_6H_6(H_2PO_4)_6$ known as inositol hexakisphosphate or phytate in salt form, is the principal storage form of phosphorus.[28] Phytic acid is a green, non-toxic, and environmentally beneficial substance that can be widely isolated from plants.[29]

Herein, by merely employing melamine as a self-sacrificial template for surface synthesis and pyrolysis technology, we created a distinctive porous carbon sheet. The produced PCSs have a rich composition of doped oxygen, phosphorus, and nitrogen, a 2D shape, a large specific surface area, and a high mesopore/micropore density. The large-area and extremely porous structure produce strong physical sulfur confinement, abundant active surfaces, and excellent long-range conductivity when utilized as a sulfur host. More significantly, this highly porous structure introduces a connected porous framework for ion transfer through a carbon matrix, which overcomes graphene's slow vertical ion conductivity and achieves rapid ion transfer in the electrode, realizing quick and effective sulfur electrochemistry. In addition, the abundant N, P, and O doping in the carbon lattice contributes to a significantly polarized surface, strengthening the favorable chemical interaction between the carbon material and the sulfur species and further fixing the sulfur. Due to these outstanding advantages, the PCS900 sulfur electrode achieves excellent electrochemical performance, presenting a high initial capacity of 949 mA h g^{-1} at 838 mA g^{-1}, and maintaining 652 mA h g^{-1} after 200 cycles with a decay of 0.156% per cycle. In 1000 cycles, the capacity decay rate per cycle is 0.079%, and a high sulfur content up to 83.5 wt% is observed.

2. Experimental section

2.1 Synthesis of PCS800, PCS900, and PCS1000

PCS900 was prepared by calcination using melamine as a carbon source and phytic acid as a single template. Typically, 2.0 g phytic acid (Aladdin) was dissolved in 40.0 mL deionized water with continuous stirring and 2.0 g melamine (Aladdin) as a carbon source was added (in a weight ratio of 2 : 2). The mixed solution was stirred for 12 hours, and then transferred to an 80 °C oven for 24 hours to evaporate water. The obtained powder was transferred to a tube furnace under an N_2 atmosphere and pyrolyzed at 800 °C and 900 °C for 1 and 3 h, respectively, at a rate of 3 °C min^{-1}. Synthesis at different pyrolysis temperatures (800 °C for 4 h, 800 °C and 1000 °C for 1 and 3 h, respectively) was also carried out to obtain PCS800 and PCS1000 and to study their influence on the morphology and structure.

Synthesis with different melamine to phytic acid ratios of 2 : 2 and 2 : 4 was also performed through the same procedures to study their effects on the morphology and structure of the obtained PCS.

2.2 Synthesis of PCS800/S, PCS900/S, and PCS1000/S

Carbon–sulfur composite materials were prepared by conventional melt-diffusion approaches. The composite materials (PCS800, PCS900, and PCS1000) and sublimated sulfur were mixed homogeneously at a weight ratio of 1 : 6. The mixture was heated at 155 °C for 10 h, and then heated to 220 °C for

30 min. The resulting samples were denoted as PCS800/S, PCS900/S and PCS1000/S, respectively.

2.3 Materials and characterization methods

The phase and crystallites were characterized by X-ray diffraction (XRD, Bruker D8 Advance, with Cu K_α (λ = 0.154 nm) radiation at 40 kV and 40 mA, Germany). The morphology of the materials was imaged by scanning electron microscopy (SEM), which was performed on FEI QUANTA FEG 450 with 10 kV, and transmission electron microscopy (TEM, Talos F200X, FEI, USA). The N_2 adsorption/desorption isotherms and the BET surface area (SBET) were determined using Quantachrome Instruments Autosorb-iQ2 which was equipped with a liquid nitrogen bath to keep the temperature at 77 K. The Brunauer–Emmett–Teller (BET) method was used to calculate the specific surface area, and the relative pressure range of P/P_o of 0.01–0.2 was used for BET analysis, and the pore-size distributions were calculated based on the DFT method. The chemical state of elements was investigated using X-ray photoelectron spectroscopy (XPS) and Raman spectroscopy (Thermo Scientific DXRxi, England) with an excitation wavelength of 514 nm. *In situ* XRD measurements were performed in a steel Swagelok-type cell. The cell was connected to a multichannel battery testing system (Neware, China).

2.4 Electrochemical measurements

Electrochemical measurements were performed in a coil-type cell. PCS/S, a conductive agent (Super P) and polyvinylidene fluoride (PVDF) were dissolved in a weight ratio of 80 : 10 : 10 in *N*-methyl-2-pyrrolidone (NMP). The mixed slurry was coated on aluminum foil and then vacuum dried at 60 °C for 12 hours. The electrode was cut and pressed into a 1.0 cm^2 disc. The average sulfur mass loading density was between 1.4 and 1.6 mg cm^{-2}. Each coin cell (2025 type) was assembled using pure Li as the anode and a Celgard 2400 sheet as the separator in a high-purity argon-filled glove box with moisture and oxygen concentrations below 1 ppm. The electrolyte consisted of 1 M lithium bis(trifluoromethanesulfonyl) imide (LiTFSI) in a mixture of DOL/DME (1 : 1 v/v) with 1 wt% $LiNO_3$, and the volume of the electrolyte in coin cells was controlled around 30 μL. The galvanostatic charge–discharge performance was measured using a battery tester (BTS3000, Neware, China) between 2.8 and 1.7 V (*vs.* Li/Li^+) at current densities based on the weight of sulfur (1 C = 1675 mA g^{-1}) at room temperature (25 °C).

Heat generation flow was measured *in operando* using a TAM isothermal calorimeter at 25 °C. The difference of heat (positive in the case of exothermic reactions and negative in the case of endothermic reactions) was measured (Seebeck sensor at the bottom of the chamber), being representative of the cell heat flow. As the reference is calibrated to 0 W before the experiment, we could directly obtain the heat flow of the cell, which is the sum of all heat produced or consumed by the cell. Due to the large volume of the chamber and the heat dissipation in the volume, some delay was observed between heat generation and its measurement by the equipment (about 15 min). The button batteries were assembled and placed in a calorimeter after 12 hours of rest. To follow heat generation during charge/discharge, the chamber was equipped with two hermetic wires for electrical connection of the cell. Li–S cells were then galvanostatically cycled in the 1.7–2.8 V voltage range.

2.5 Adsorption test

Li_2S_6 was obtained by mixing sublimated sulfur and Li_2S (99.9%) at a ratio of 5 : 1 and 1 M lithium bis(trifluoromethanesulfonyl) imide (LiTFSI) in DOL/DME (1 : 1 v/v) with 1 wt% $LiNO_3$. After heating at 65 °C overnight, the concentration was 3 mmol L^{-1}. Adsorption experiments were carried out on four different samples. 20 mg of PCS800, PCS900, and PCS1000 were added into 3 mL of Li_2S_6 solution and mixed vigorously. After thorough stirring and 24 hours standing, the mixture was placed into a glove box for observation, and then the absorption spectrum was recorded with a UV spectrophotometer (Shimadzu UV-2600).

2.6 Density functional theory calculations

All of the density functional theory (DFT) calculations were performed *via* the Vienna *Ab initio* Simulation Package (VASP).[30] The projected augmented wave method was used to describe the ion–electron interactions, in which the Perdew–Burke–Ernzerhof exchange–correlation functional was used within the generalized gradient approximation.[31,32] A cut-off energy of 500 eV was applied for all the energy and electronic calculations. A Gaussian smearing of 0.2 eV was used for structural optimization. During optimization, all atoms were allowed to relax until the final energy and forces on each atom reached 1×10^{-5} eV and 0.02 eV $Å^{-1}$, respectively. The dispersion-corrected density functional theory (DFT-D2) method in the Grimme scheme has been used in all the calculations.[33] A vacuum of 15 Å separates surface images in the *Z*-direction. The Brillouin-zone was sampled using the gamma centered Monkhorst–Pack method with a 3 × 3 × 1 *k*-point mesh for energy calculations and 5 × 5 × 1 *k*-point mesh for the electronic structure. The binding energy E_b of Li_2S_n on PCS900 was obtained by the equation, $E_b = E_{LG} - E_G - E_L$, where E_{LG}, E_G, and E_L represent the total energy of Li_2S_n@PCS900, PCS900, and Li_2S_n, respectively. In this work, we chose two defective PCS900 with N,P-substitution named pyridinic-like PCS900 (PI/PCS900-P) and pyrrolic-like PCS900 (PR/PCS900-P), respectively.

3. Results and discussion

Fig. 1 illustrates the preparation process of PCS900 and the synthesis of sulfur to be loaded. In this work, melamine and phytic acid were mixed in a weight ratio of 1 : 1, and then the obtained powder product was pyrolyzed at 800 °C and 900 °C for 1 h and 3 h, respectively, under a nitrogen atmosphere. The phytic acid-doped melamine transforms into a porous sheet-like morphology and forms an interconnected network

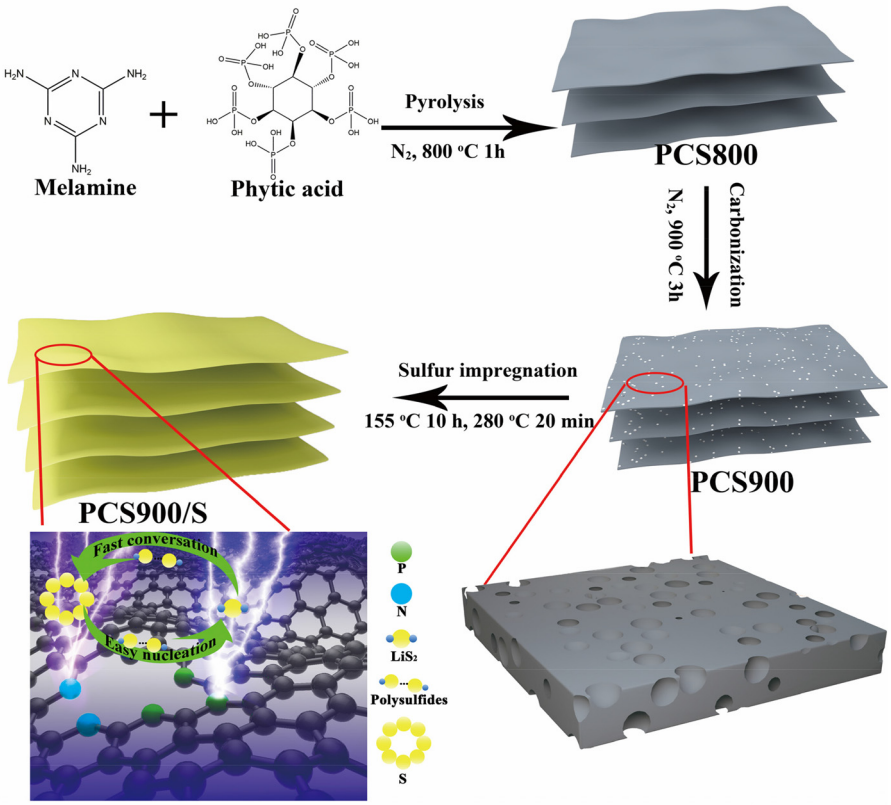

Fig. 1 Schematic representation of the preparation of PCS900 and PCS900/S composites.

at the same time. During the heating process, phytic acid plays a key role in the synthesis of PCS900, not only as a rich phosphorus source for doping, but also as a pore former to form rich porous structures during high temperature pyrolysis. Numerous micropores and mesopores were produced during the pyrolysis of phytic acid, and the resulting porous network structure was able to successfully prevent the dissolution of soluble polysulfides. More crucially, these highly porous carbon nanosheets are woven together into a porous structure that speeds up ion transit, overcomes poor vertical ionic conductivity, and encourages the electrochemical reaction of sulfur. In addition to providing increased pore volume for large sulfur loadings, controlling porosity and specific surface area by pyrolysis temperature also creates channels for multidirectional ion transport.

Fig. 2(a and b) exhibits the micromorphology of PCS800, which is in the shape of a block. PCS900 images (Fig. 2c) vividly describe the microstructure, which is a sheet-like morphology. It demonstrates that the porous sheet structure cannot be generated at 800 °C, which is due to insufficient phytic acid pyrolysis and insufficient melamine etching. In PCS900 and PCS1000, two-dimensional sheet-like structures can be seen, showing that phytic acid pyrolysis efficiently promotes the development of sheet-like materials and prevents melamine from agglomerating. Scanning transmission electron microscopy was used to further validate the linked porous architecture, as seen in Fig. 2d (STEM). The resultant PCS900 (Fig. 2d), in stark contrast to the morphology of PCS800 (Fig. 2b), displays a large number of disorganized holes dispersed throughout the porous architecture. It has also been demonstrated that high temperatures encourage the development of porous structures. The porous sheet-like materials are interlaced to create a porous structural framework carbon material, which increases the material's electrical conductivity by facilitating the passage of electrons and ions on the surface. The resulting PCS900 has an amorphous structure, as seen from the selected area diffraction (SAD) pattern in the inset of Fig. 2d, where no conspicuous diffraction rings were seen. The micromorphology of PCS1000, which resembles that of PCS900 slightly, is shown in Fig. 2e and f. Fig. S3† depicts the microstructures with 2 : 2 and 2 : 4 melamine to phytic acid ratios. As the phytic acid ratio rises, the size of the porous carbon sheet also rises. To investigate their impact on the shape and structure of the produced PCS, the same techniques were used to synthesize the material with different melamine to phytic acid ratios of 2 : 2 and 2 : 4. Fig. 2g shows the micromorphology of PCS900/S after sulfur impregnation. The high-angle annular dark-field (HAADF) image (Fig. 2h) and elemental mapping images (Fig. 2i–m), show that C, N, O, P, and S elements are uniformly distributed in the PCS900 host.

The XRD patterns of PCS800, PCS900, PCS1000, PCS900/S, and sulfur are presented in Fig. S1 (ESI†). There are two broad diffraction peaks located at approximately 30 and 45° in

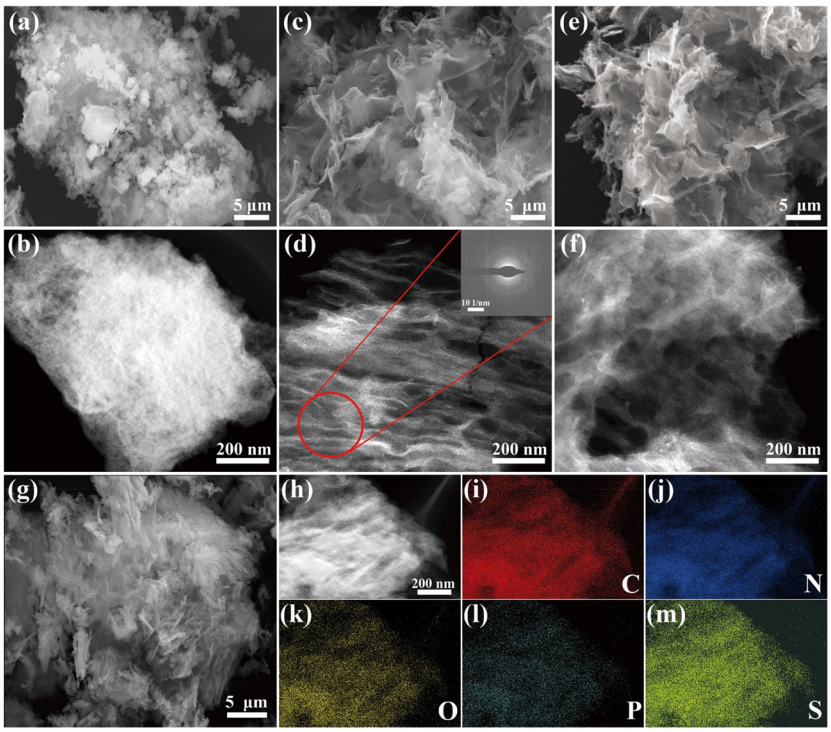

Fig. 2 SEM and HAADF images of PCS800 (a and b), PCS900 (c and d), PCS1000 (e and f), and PCS900/S (g and h); SAD (inset) images of PCS900 (d); elemental mapping of C, N, O, P, and S (h–m).

PCS900 and PCS1000, indicating the amorphous structure of carbon. The sublimated sulfur exists in an orthorhombic structure (S_8, JCPDS no. 08-0247). The distinctive peak of sulfur in PCS900/S is drastically reduced when sublimated sulfur melts into the carbon composite material, showing that the sulfur is uniformly confined in the pores of PCS900. The thermal stability of sulfur and the sulfur content in the PCS900/S composite are 83.5 wt%, according to thermogravimetric analysis (TGA). The evaporation of sulfur in the macropores of the composite, as shown in Fig. S2 (ESI†), causes the curve to drop sharply in the temperature range of 160–250 °C. The continued weight loss of the curve at 250–320 °C is attributed to the evaporation of the sulfur remaining in the mesopores of the composites. Then the weight loss between 320 °C and 400 °C resulted from the evaporation of sulfur in the micropores of the composite, indicating that sulfur is well confined in PCS900. N_2 adsorption/desorption measurements were performed to investigate the specific surface area and pore size distribution of PCS800, PCS900 and PCS1000. As shown in Fig. 3a, the isotherm of PCS900 and PCS1000 exhibits high adsorption at low relative pressures and a typical hysteresis loop at medium relative pressure, indicating the existing hierarchical structure, especially abundance of mesopores and micropores. As shown in Table 1, the specific surface area and pore volume increase with the increase of temperature, while the contents of phosphorus and nitrogen follow an opposite trend. The Brunauer–Emmett–Teller (BET) surface area of PCS900 was found to be 2816.12 $m^2\ g^{-1}$ and a high pore volume of 2.82 $cm^3\ g^{-1}$ was observed, which are overwhelmingly higher than those of PCS800 (79.2 $m^2\ g^{-1}$ and 0.29 $cm^3\ g^{-1}$, respectively). The porosity of PCS900 in Fig. 3a is also supported by the obvious peaks of pore size distribution at 0.3–4.0 nm.

The pore size distribution and N_2 sorption isotherms of PCS800, on the other hand, show that this material has a substantially lower porosity and specific surface area than PCS900, which is consistent with the TEM results. There are two reasons for PCS900's high porosity: (i) during the first stage of the pyrolysis process at 800 °C, the phosphoric acid produced by decomposition continuously corrodes the carbon skeleton to form a microporous structure and (ii) during the second stage of the pyrolysis process at 900 °C, the remaining phytic acid and phosphoric acid were reduced by carbon to red phosphorus, resulting in sublimation and leaving a significant amount of mesopores and micropores in the product. The microstructures of PCS800, PCS900 and PCS1000 composites were further analyzed by Raman spectroscopy (Fig. 3b). Two evident peaks at 1345 and 1580 cm^{-1} in all the specimens can be assigned to the breathing modes of the hybrid carbon rings (D band) and graphitic sp^2 stretching of graphene (G band), in addition to a 2D band at about 2700 cm^{-1}.[34] The D-band and G-band area ratios (I_D/I_G) of PCS900 and PCS1000 are 1.03 and 1.05, respectively, which are lower than those of PCS800 (2.69), indicating that the heterogeneous atom doping structures of PCS900 and PCS1000 are similar. Moreover, a bump near 2700 cm^{-1} in the Raman spectrum of PCS800 compared to that of PCS900 indicates a higher sheet thickness, which is

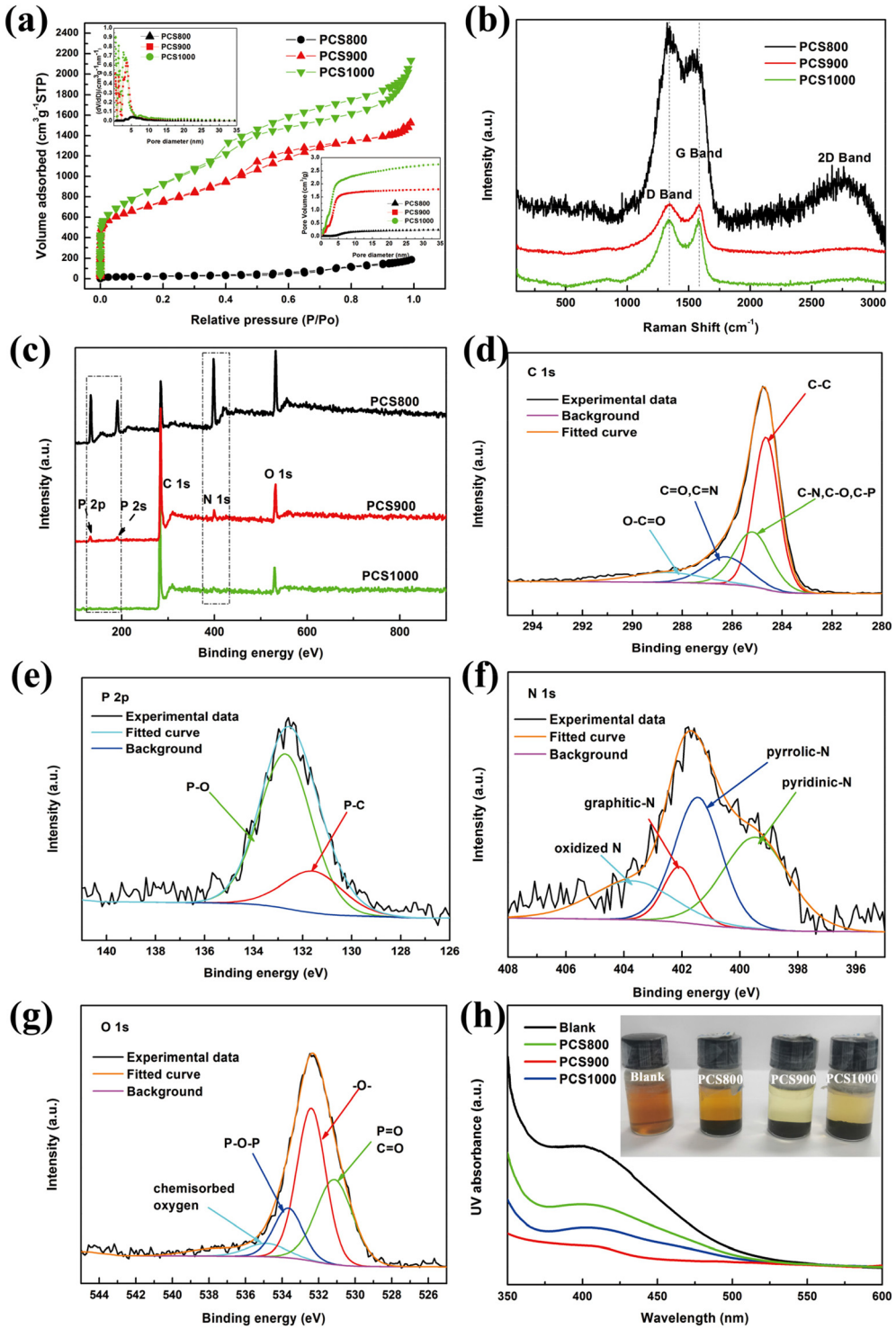

Fig. 3 N_2 adsorption–desorption isotherms, cumulative plot of the pore size distributions (inset) (a), Raman spectra (b), and the overall XPS spectra of PCS800, PCS900, and PCS1000 (c); C 1s (d), P 2p (e), N 1s (f), and O 1s (g) spectra of PCS900; the ultraviolet/visible spectra and photograph of polysulfide solutions of adsorbed PCS800, PCS900, and PCS1000 (h).

consistent with previous TEM results. The porosity and specific surface area of PCS900 are significantly higher compared to those of PCS800, which is consistent with N_2 adsorption/desorption measurement results.[35]

The chemical composition of PCS800, PCS900 and PCS1000 was further examined by X-ray photoelectron spectroscopy (XPS). The elemental survey spectra are displayed in Fig. 3c. The PCS800, PCS900, and PCS1000 samples have five peaks at

Table 1 Porous carbon sheet parameters of nitrogen adsorption–desorption, Raman spectroscopy and nitrogen content

Sample	Specific surface area ($m^2\ g^{-1}$)	Pore size (nm)	Pore volume ($cm^3\ g^{-1}$)	*P* (at%)	*N* (at%)
PCS800	79.2	1.47	0.29	25.6	20.1
PCS900	2816.1	3.82	2.82	4.8	5.2
PCS1000	3087.9	3.99	3.07	0.8	0.5

284.6, 400.2, 531.6, 132.8 and 190.5 eV, which can be assigned to C 1s, N 1s, O 1s, P 2p, and P 2s, respectively. The high-resolution peaks in the C1s spectra (Fig. 3d) could be assigned to C–C (284.8 eV), C–N/C–O/C–P (285.5 ± 0.1 eV), C═O/C═N (286.5 ± 0.1 eV) and O–C═O (288.9 ± 0.1 eV), respectively.[36] The P 2p peaks (Fig. 3e) of PCS900 located at 131.7 and 132.5 eV are attributed to the P–C and P–O bonds, respectively. Fig. 3f shows the N 1s spectra of PCS900 composites, which can be divided into pyridinic N (399.4 ± 0.2 eV), pyrrolic N (401.3 ± 0.2 eV), graphitic N (402.1 ± 0.2 eV) and oxidized N (403.8 ± 0.2 eV) doped in carbon.[37] Meanwhile, the high-resolution peaks in the O 1s spectra (Fig. 3g) could be fitted into four peaks assigned to the P═O/C═O (531.0 eV), –O– (532.5 eV), and P–O–P (533.6 eV) bonds, as well as the chemisorbed oxygen (535.4 eV).[38] These results confirm that P and N are successfully doped into the carbon lattice.[39] To verify their polysulfide absorption capacity, the three samples (PCS800, PCS900, and PCS1000) were soaked in Li_2S_6 (3 mmol L^{-1}) solution for 48 h. The inset image in Fig. 3h demonstrates how adding PCS900 changed the hue of the solution from brown to colorless. In comparison, the solution becomes a lighter shade of yellow after the addition of PCS800 and PCS1000. After adding several sample powders, a UV-vis absorption test was conducted in the meantime. The absorbance peaks of the polysulfide solution containing PCS900 are much lower than those of the solutions containing PCS800, PCS900, and PCS1000, as shown in Fig. 3h. These observations show that PCSs with active nitrogen and phosphorus co-doping have a potent capacity for adsorbing polysulfides.

To study the detailed reaction during the discharge/charge process, *in situ* XRD patterns (2θ = 20°~35°) and *in operando* microcalorimetry measurements were acquired during the first discharge/charge test (Fig. 4). According to the lithiation curve, the reaction equations of polysulfides during discharge is as follows.[40,41] The colored patterns in Fig. 4b and c represent the four regions in the Li–S battery cycle process, corresponding to the colored dots in Fig. 4a, representing different charging and discharging states.

Region I: solid sulfur is dissolved and reduced to Li_2S_8

$$2Li + S_{8(s)} \leftrightarrow 2Li^+ + S^2_{8(l)} \quad (1)$$

Region II: Li_2S_8 is reduced to long-chain polysulfides

$$2Li + 3/4S_{8(l)}{}^2 \leftrightarrow 2Li^+ + S_{6(l)}{}^2 \quad (2)$$

$$2Li + 2/3S_{6(l)}{}^2 \leftrightarrow 2Li^+ + S_{4(l)}{}^2 \quad (3)$$

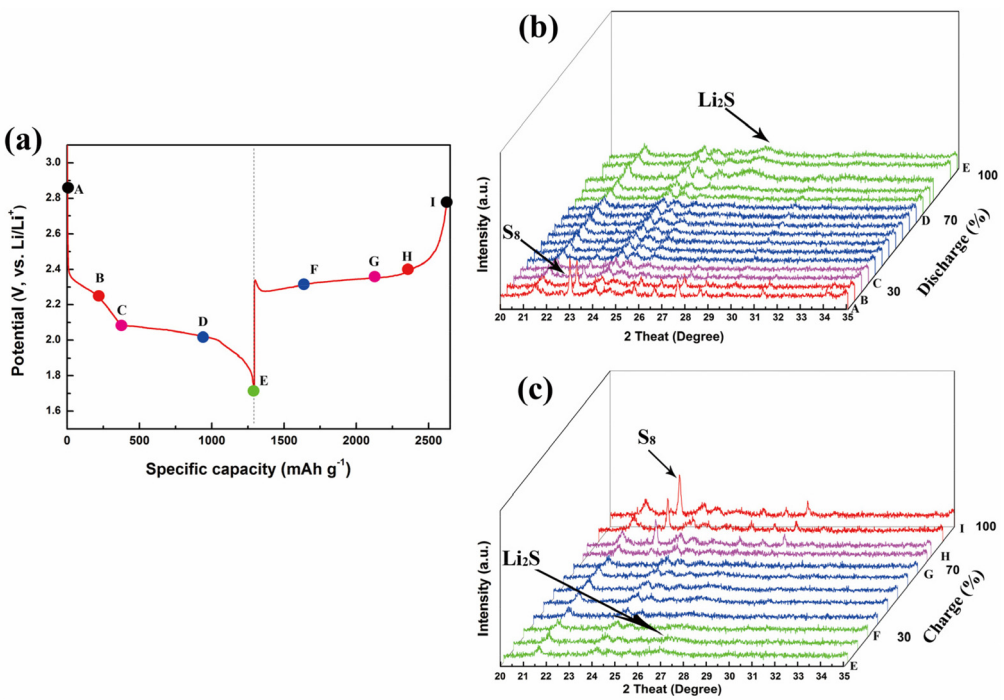

Fig. 4 Typical galvanostatic curve of the PCS900/S cathode at a rate of 0.1 C (a), Waterfall representation of *in situ* XRD data at different discharge (b) and charge (c) states.

Region III: long-chain polysulfides are reduced to short-chain polysulfides

$$2Li + S_{4(l)}{}^{2} \leftrightarrow 2Li^{+} + S_{2(l)}{}^{2} \quad (4)$$

$$2Li + 1/2S_{2(l)}{}^{2} \leftrightarrow 2Li^{+} + S_{(l)}{}^{2} \quad (5)$$

Region IV: Li_2S_2 and Li_2S are reduced to $Li_2S_{(s)}$

$$2Li^{+1} + 1/2S_{2(l)}{}^{2} \leftrightarrow Li_2S_{(s)} \quad (6)$$

$$2Li^{+1} + S_{(l)}{}^{2} \leftrightarrow Li_2S_{(s)} \quad (7)$$

Once the discharge starts, the characteristic crystallization peaks (23.1°) of sulfur (JCPDS no. 08-0247) gradually weaken (Fig. 4b). As $S_{8(l)}$ is reacted, the concentration of $S_{8(l)}$ in the electrolyte decreases, promoting the dissolution of $S_{8(s)}$ into $S_{8(l)}$.[42] This demonstrated the rapid conversion from elemental sulfur to long-chain polysulfides (eqn (1) and (2)). The discharge depth is from 30 to 70%, and the sharp peaks of α-S_8 at 23.1°, 25.8°, 26.7°, 27.7°, and 28.6° gradually disappeared, which corresponds to the formation of long-chain polysulfides (eqn (2) and (3)).[43] At the same time, the short-chain polysulfides ($S_{2(l)}{}^{2}$ and $S_{(l)}{}^{2}$) start to be reduced (eqn (4) and (5)) and the concentration of the long-chain polysulfides ($S_{8(l)}{}^{2}$, $S_{6(l)}{}^{2}$, and $S_{4(l)}{}^{2}$) decreases. The discharge depth is from 70 to 100%, and a new broad peak appears at ~27°, which is attributed to the formation of cubic Li_2S (JCPDS no. 23-0369). Meanwhile, at the end of the discharge step, the Li_2S peak intensity continues to increase and its full width at high maximum (FWHM) is about 0.95°, which indicates that the Li_2S crystallites are micron-sized.[40] This observation is consistent with expectations, and finally a solid product Li_2S is formed.

At the beginning of the charging process (Fig. 4c), the Li_2S peak (111) intensity gradually decreases due to the reaction of long-chain polysulfides ($S_{8(l)}{}^{2}$, $S_{6(l)}{}^{2}$, and $S_{4(l)}{}^{2}$). The reverse reactions (eqn (5) and (4)) at this stage from F to G mainly contribute to further delithiation. Additionally, no crystalline Li_2S peak was found from G to H, corresponding to the reverse reaction (eqn (3) − eqn (1)) for some polysulfides dissolved in the electrolyte. During the discharge from H to I (Fig. 4c), the new sharp peaks of crystalline sulfur are around 23.1°, 25.8°, 26.7°, 27.7° and 28.6°, which are designated as the crystallization peaks of sulfur (JCPDS no. 08-0247).[44]

The intermediate polysulfides in the electrolyte are typically in a liquid state and challenging to find during the cycling process. We performed *in operando* microcalorimetry measurements to look into the phenomenon of heat generation during the electrochemical reaction inside the Li–S batteries (Fig. 5). As per literature survey,[45] many *in situ* characterization studies (*in situ*/*operando* synchrotron-based techniques[46] and *in situ* Raman spectroscopy[47]) were used to explore the intermediate polysulfides of Li–S batteries, but few were used in *in operando* microcalorimetry. We assembled a button battery with sufficient lithium and electrolyte, a sulfur content of 1.4–1.6 mg cm ^{2}, and current densities of 0.1 and 1 C to measure the heat flow during the galvanostatic cycling process.

The voltage steadily drops and the heat flow increases once the discharge begins at 0.1 C (Fig. 5). The difference between the heat flow curve at 0.5 C and the current density at 0.1 C is explained by the more potent multi-step reaction of polysulfides. This suggests that the multi-step electrochemical process is influenced by the current density, and that the more complete the reaction, the smaller the current. Fig. 5 demon-

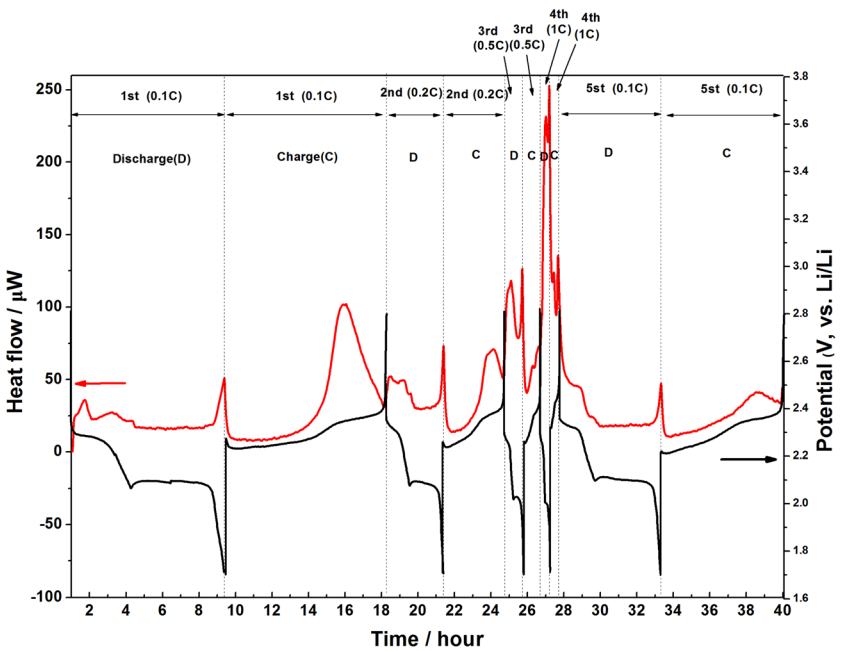

Fig. 5 Experimental charge–discharge profiles (black line) and heat flow generation (red line) of the PCS900/S electrode cycled at 0.1 C to 1 C.

strates that the creation of polysulfides (Li_2S_8 and Li_2S_6) and the dissolution of sulfur are both accompanied by the first plateau at 2.30 V, which is also accompanied by a significant heat flow peak.[48] Following the first heat flow peak, another heat flow peak appeared, possibly due to the heat flow generated by the complete transfer of solid sulfur into solution and reduction to long-chain polysulfides. When the voltage drops to 2.1 V during the discharge plateau, the heat flow curve declines slowly, which can be attributed to the reduction of long-chain polysulfides to short-chain polysulfides.[49] Subsequently, the heat flow curve was smooth during the short-chain polysulfide reaction, and the heat flow hardly increased or decreased. It can be considered that the soluble polysulfides (Li_2S_4) generate insoluble polysulfides (Li_2S_2).[50] At the end of the discharge, the sudden increase in heat flow at the end of the discharge can be attributed to the increase in battery polarization,[51] and the increase in resistance and heat release could be caused by the deposition of Li_2S insulation on the electrode surface. At the same time, the heat flow curves of discharge under different current densities are compared, and the results show that when the current density is higher, more heat is generated during the discharge process. When the current density is discharged at 1 C, the heat flow reaches a maximum value of 250 μW.

During the charging process, the heat flow curve with a current density of 0.1 C has a large heat flow peak. Through *in situ* XRD characterization, it can be concluded that this peak indicates the release of a large amount of heat when short-chain polysulfides react to form long-chain polysulfides (Li_2S_x, $4 \leq x \leq 8$). Comparing the heat flow curves of 0.1 C, 0.2 C, 0.5 C and 1 C charging processes, the released heat during the charging process decreases when the current is larger. This indicates that the electrochemical reaction during charging is incomplete at higher currents, resulting in a less exothermic nature. This indicates that the complete reaction of short-chain polysulfides (Li_2S_x, $4 \leq x \leq 6$) is important for improving the efficiency of sulfur electrodes. The result of heat generation is of great significance to combine *in operando* microcalorimetry techniques to reveal the complex reaction mechanism of sulfur electrodes in Li–S batteries. Combined with *in situ* XRD and heat flow curves, long-chain polysulfides are found to be the primary incomplete reactants, according to the evidence. While using a small current for charging and discharging, more heat is released during the charging process than during the discharging process; when using a large current for charging and discharging, more heat is released during the discharging phase than during the charging process. To increase the effectiveness of sulfur electrodes, the conversion reaction of long-chain polysulfides is therefore crucial. It is extremely important to reveal that the intricate reaction mechanism of sulfur electrodes in lithium–sulfur batteries that these results are consistent with *in situ* XRD measurements. The data that were obtained are crucial for understanding how well lithium–sulfur batteries perform in terms of safety.

For practical use, it is useful to simulate the heat generated by lithium–sulfur battery charging and discharging. Therefore, the study of the battery's thermal effect establishes the groundwork for the creation of a safe and dependable energy storage system by offering a theoretical basis for the battery's thermal management. Heat is typically produced during the charging and discharging of the battery. When heat cannot be expelled, it will build up and increase the temperature. The battery system will experience thermal runaway at high temperatures. As a result, battery thermal simulation aids in understanding its heating effect and enhances battery performance. In order to investigate the battery heat generation and temperature fluctuations, we thermally model the battery charging and discharging process using finite element software. In this experiment, the battery was simulated under a rate test, and a computation was made to determine the change curve of battery temperature over time.

As shown in Fig. 6, a 2025 battery model structure was built. The thickness of the battery is 2.5 mm (averagely divided into 4 layers) and the diameter is 10 mm. We consider the battery as an isolated system that undergoes only heat transfer without any material exchange with the external environment.

The heat generated during the battery discharge process is mainly Joule heat, and the heat inside the battery is uniform. The heating density formula is:

$$Q = I(U_{OCV} - U_{WV})/V \tag{8}$$

where Q is the heat generation density; I is the current; U_{OCV} is the open circuit voltage; U_{WV} is the working voltage; and V is the battery volume.

According to the law of conservation of energy, the heat calculation formula of the model is:

$$\rho C_p \frac{\partial T}{\partial t} = k\nabla T + Q \tag{9}$$

where ρ is the density of the electrode material; C_p is the specific heat capacity; Q is the heat generation density; T is the temperature of the battery surface; t is the time; and k is the

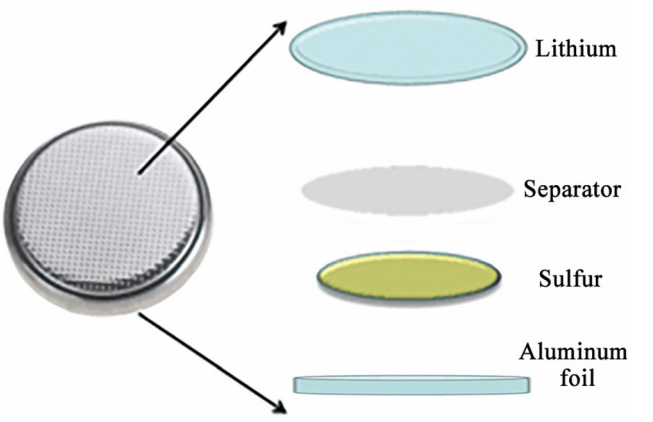

Fig. 6 Schematic illustration of the model of the PCS900/S cell.

thermal conductivity. The thermodynamic parameters of the battery model materials are shown in Table 2.

We made the following assumptions for the battery model: (1) thermal radiation is not considered; (2) heat is uniformly transferred on the electrode surface; and (3) the battery surface is in contact with air at a constant temperature (298.15 K).

The first type of boundary condition for the battery model:

$$T = 298.15\ \text{K}. \tag{10}$$

Table 2 The thermodynamic parameters of battery materials[52]

Materials	Specific heat capacity /J (kg K)$^{-1}$	Thermal conductivity /W (m k)$^{-1}$	Material density /kg m^{-3}
Lithium	3600	84.80	530
Separator	1978	0.33	1008
Sulfur	1269	1.58	2328
Aluminum foil	900	238.00	2700

The second type of boundary condition for the battery model:

$$-k_1 \frac{\partial T}{\partial n} = -k_2 \frac{\partial T}{\partial n}$$

Among them, k_1 and k_2 are the thermal conductivities of the material, as shown in Table 2.

As shown in Fig. 7a, the temperature distribution inside the battery is simulated under constant temperature conditions. The battery was charged and discharged, and the heat flow curve at the current density from 0.1 C, 0.2 C, and 0.5 C to 1 C was obtained using an isothermal meter, and then the temperature change from the inside to the outside of the battery was simulated by the heat flow. Fig. 7a shows that the battery's temperature steadily rises from the outside to the interior, with the positive electrode having the majority of the battery's high internal temperature. Fig. 7b depicts the simulation of the cell temperature under excessive sulfur loading. Under constant temperature conditions, as the sulfur content increases, the temperature of the battery from the inside to the outside also increases, and when the cathode is loaded with

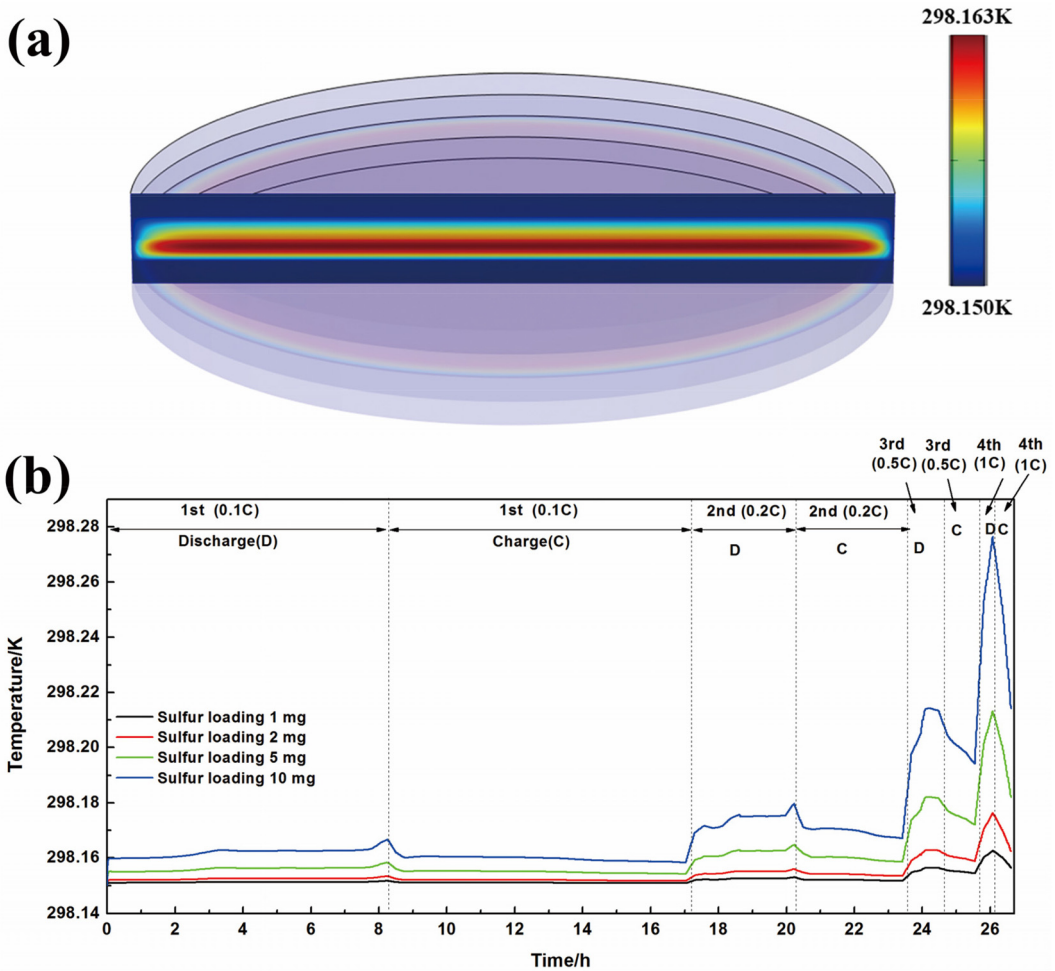

Fig. 7 Temperature distribution of the cell after the rate test at constant temperature (a) and temperature simulation image of the cell with different sulfur loadings (b).

10 mg sulfur, the battery temperature rises by about 0.13 °C. Comparing the changes of battery temperature during charging and discharging shows that the temperature rise in the charging process is greater than that in the discharging process at a current density of 0.1 C; the temperature rise in the discharging process is greater than that in the charging process at a current density of 1 C. These insights further clarify the connection between temperature and current in lithium–sulfur batteries during charging and discharging and offer a foundation for thermal management of lithium–sulfur batteries by simulating the temperature of lithium–sulfur batteries *via* heat flow.

To elucidate the effect of N,P-substitution in the PCS900 composite, the binding energies between PCS900 and polysulfide species were calculated using density functional theory (DFT). The optimized equilibrium structures of Li_2S_n@PI/PCS900-P and Li_2S_n@PR/PCS900-P are shown in Fig. 8(b and c). The binding energies of Li_2S, Li_2S_2, Li_2S_4, Li_2S_6, and Li_2S_8 species to PI/PCS900-P are calculated to be 6.18, −4.97, −4.46, −3.87, and −3.70 eV, respectively, as shown in Fig. 8a. These values are much higher than those of the N-substituted graphene,[53] suggesting that the chemical anchoring of polysulfides is strengthened by the introduction of a phosphorus atom. The chemical adsorption mainly originates from the double interactions: chemical bonding between P and S atoms, and chemical bonding between Li and N. Take Li_2S as an example; the Li–N bond distance is around 1.81 Å, and the S–P bond distance is only 2 Å. Based on the above calculation results, the coexistence of strong Li–N and S–P bonds gives the N, P co-doped PCS900 with strong affinity to polysulfide species.

The PCS800/S, PCS900/S, and PCS1000/S composites were used as cathode materials for half-cell assembly to measure the electrochemical performance. The sulfur content of the cathode composites was about 83.5 wt%, and the sulfur loading was approximately 1.5 mg cm $^{-2}$. Fig. 9a shows the rate performance of the PCS800/S, PCS900/S, and PCS1000/S cathodes with increasing current densities (0.1–2 C). The initial discharge specific capacity of the PCS900/S cathode was as high as 1259 mA h g $^{-1}$ at 0.1 C, which is much higher than those of the PCS1000/S cathode (1121 mA h g $^{-1}$) and the PCS800/S cathode (387 mA h g $^{-1}$). Moreover, when the current was gradually increased from 0.1, 0.2, 0.5 and 1 C, to 2 C, the PCS900/S cathode exhibited an obvious increase in rate performance, providing specific capacities of 1259, 1087, 897, 636 and 415 mA h g $^{-1}$, respectively. After the current densities were reduced to 0.5, 0.2 and 0.1 C, reversible discharge capacities of 762, 985 and 1114 mA h g $^{-1}$ were restored, respectively, indicating that the PCS900/S cathode had excellent structural stability and better reaction kinetics. In contrast, the PCS800/S and PCS1000/S cathodes show rapid capacity decay. The charge and discharge curves of PCS800/S, PCS900/S, and PCS1000/S cathodes at different current densities of 0.1–2 C are shown in Fig. 9b. The cyclic voltammetry (CV) curves (Fig. 9c) show the typical two cathodic peaks and one anode peak of the PCS800/S, PCS900/S and PCS1000/S electrodes in the voltage range of 1.7–2.8 V at a scan rate of 0.1 mV s $^{-1}$. In the first cycle, compared with the PCS800/S and PCS1000/S electrodes, the PCS900/S electrode has a much smaller potential hysteresis in the voltage and CV curves, which means that its electrochemical polarization is smaller and the reaction kinetics is faster.

To further study the reaction kinetics of the electrochemical PCS900/S composite, we acquired electrochemical impedance spectroscopy (EIS) data (Fig. 9d). The Nyquist curves were composed of a semicircle in the high–medium frequency region

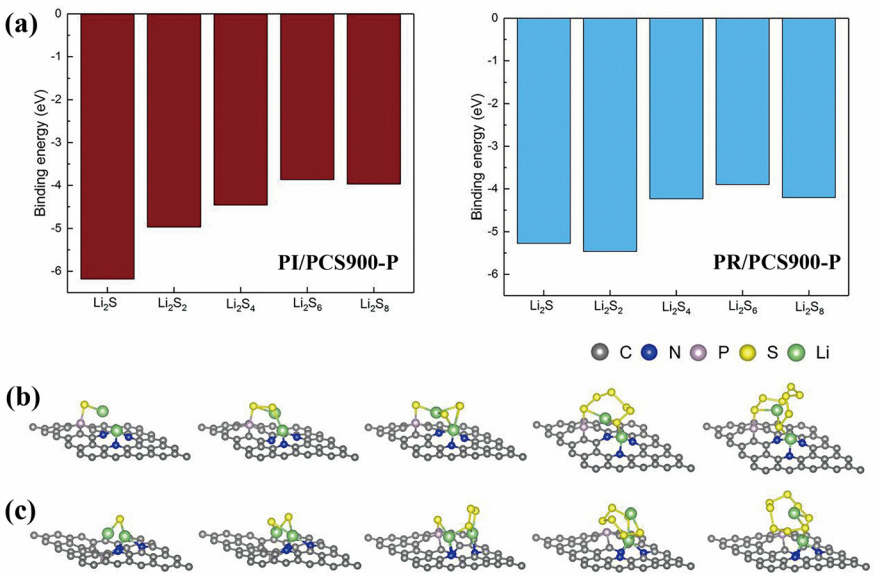

Fig. 8 Theoretical calculations of the binding energy of several sulfur species with PI/PCS900-P and PR/PCS900-P (a). The optimized equilibrium structures of Li_2S_n@PI/PCS900-P and (b) Li_2S_n@PR/PCS900-P (c).

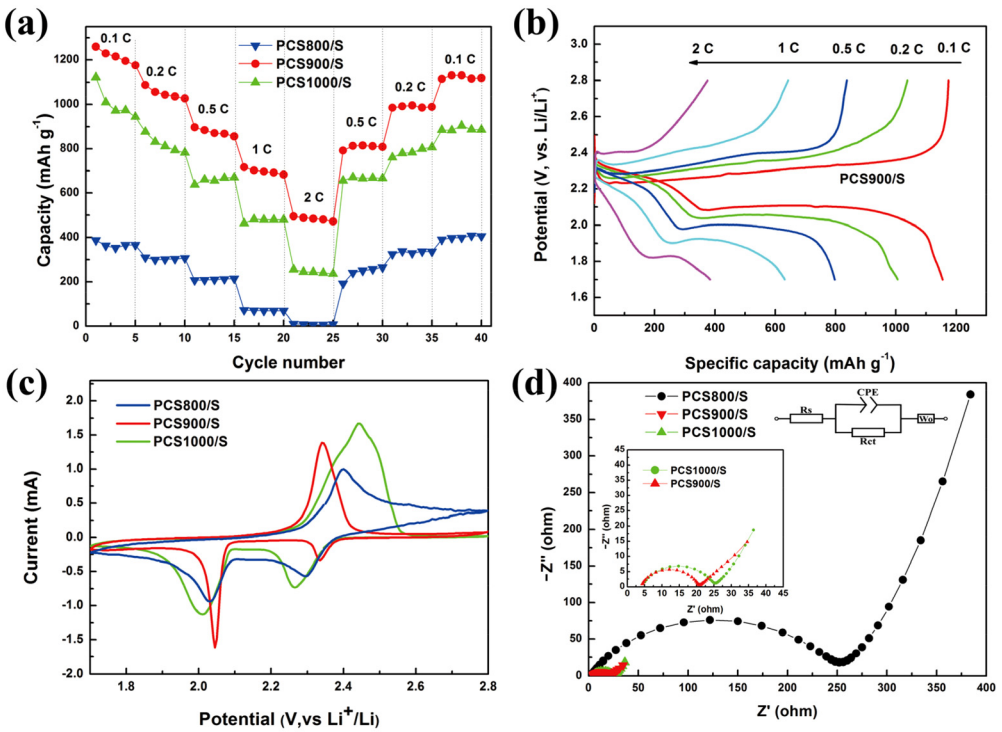

Fig. 9 Rate performances (a) and galvanostatic charge/discharge curves (b) at various current densities of the PCS800/S, PCS900/S, and PCS1000/S cells. Cyclic voltammograms of PCS900/S at 0.1 mV s^{-1} (c), and electrochemical impedance spectroscopy curves of the PCS800/S, PCS900/S, and PCS1000/S cathodes before cycling (d).

and a diagonal line in the low-frequency region. The semicircle in the high–medium frequency region is related to the charge transfer impedance at the electrode interface, which reflects the lithium-ion diffusion through the interface in contact.[54,55] The diagonal line is related to the diffusion impedance polysulfides in the electrolyte, corresponding to the Warburg impedance.[56] These Nyquist curves can be fitted using an equivalent circuit in Fig. S5 (ESI†), and the fitting results are shown in Table S1 (ESI†). The ohmic resistance (R_s) mainly reflects the resistance of the electrolyte and the current collector. Before cycling, the ohmic resistance (R_s) of the PCS900/S (4.1 Ω) and PCS1000/S (4.1 Ω) electrodes was low, indicating that the electron conductivity is significantly higher than that of the PCS1000/S (12.4 Ω) electrode. The internetwork is responsible for higher electrical conductivity. In the high–medium frequency range, a semicircle corresponding to the charge transfer resistance (R_{ct}) can be clearly defined. We found that the R_{ct} of the PCS900/S (16.4 Ω) electrode is much smaller than those of PCS1000/S (21.5 Ω) and PCS800/S (250.2 Ω) electrodes, indicating that the electrochemical kinetics is faster. These results could be attributed to the highly porous structure of the carbon network with a large surface area for charge adsorption.

Fig. 10a shows that the initial specific capacities in cycling performances of the PCS800/S, PCS900/S and PCS1000/S cathodes are 1174, 1098, and 450 mA h g^{-1}, respectively, at 0.1 C, and the average capacity decay rates correspond to 0.19, 0.21, and 0.31% per cycle, respectively. The average capacity decay rate of PCS900/S is significantly lower than those of PCS800/S and PCS1000/S cathodes. The charge and discharge curves of all three kinds of cells at current densities of 0.1 C are shown in Fig. 10b. On switching the current rate to 0.5 C (Fig. 10c), the PCS900/S cathode also demonstrated a high initial specific capacity of 949 mA h g^{-1} and a reversible specific capacity of 651 mA h g^{-1} after 200 cycles, which were much higher than those of the PCS1000/S (539 mA h g^{-1}) and PCS800/S cells (96 mA h g^{-1}). Even when the current rate increased to 1 C (Fig. 10e), the PCS900/S electrode still exhibited a high discharge capacity over 500 cycles, a capacity of 772 mA h g^{-1} after the activation of several cycles and an average capacity fading rate of 0.079% per cycle, which are much lower than those of PCS1000/S (0.14%). In contrast, the discharge capacity of the PCS1000/S electrode decreased to 200 mA h g^{-1} after 500 cycles, and the rapid capacity decay is due to poor conductivity. The PCS900/S electrode is superior to recently reported sulfur electrodes based on 2D carbon materials (Table S2, ESI†). Therefore, to further investigate high energy density Li–S batteries, high sulfur loading is a key factor. Fig. 10d shows the PCS900/S electrode with different sulfur loadings measured at 0.2 C up to 100 cycles. The PCS900/S electrode with a sulfur loading of 2.5 mg cm^{-2} yields an initial specific capacity of 997 mA h g^{-1} (2.49 mA h cm^{-2}) and is maintained at 721 mA h g^{-1} after 100 cycles. With a sulfur loading of 4.2 mg cm^{-2}, the initial specific capacity and reversible capacities were further increased to 812 mA h g^{-1} (3.41 mA h cm^{-2}). The excellent electrochemical performance of the high-

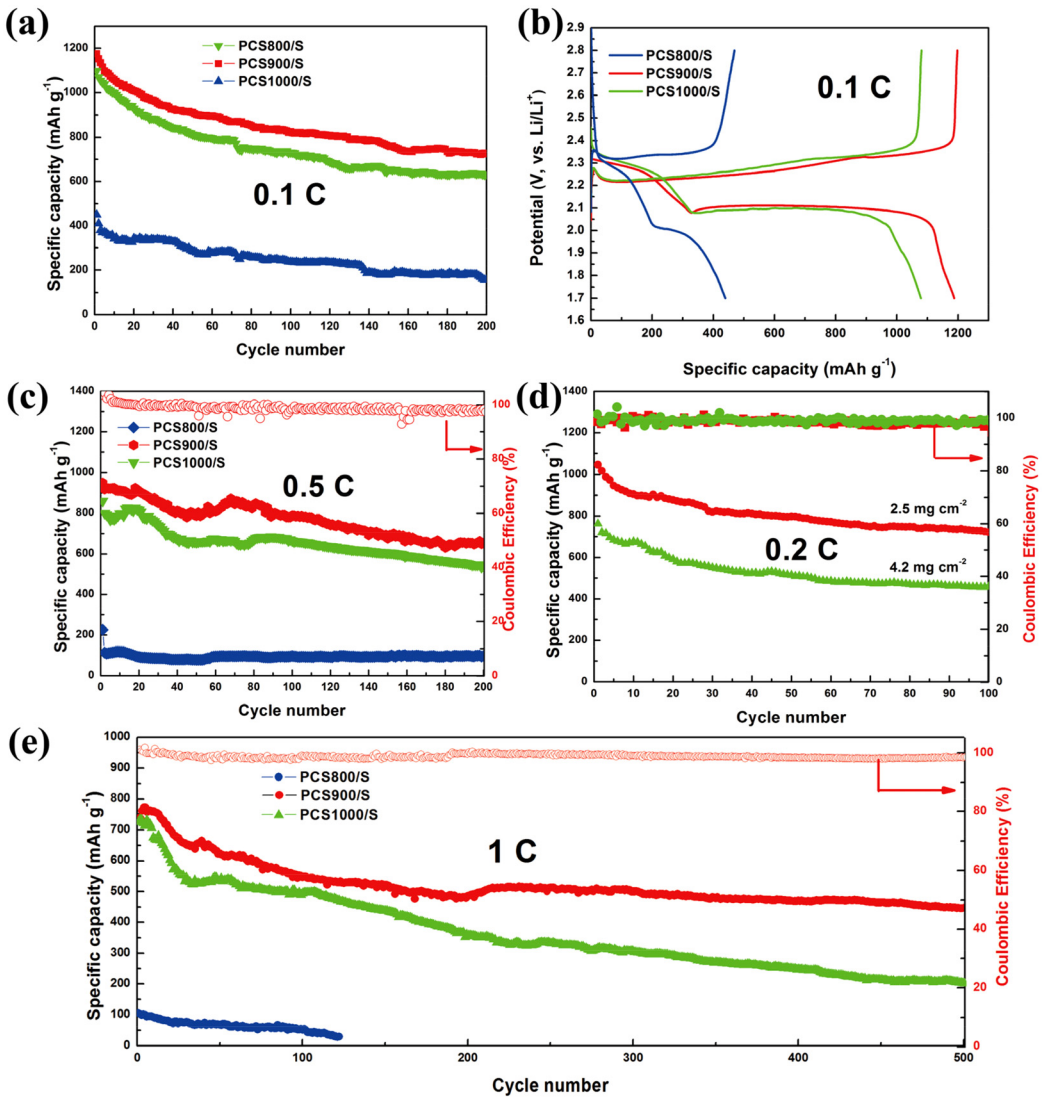

Fig. 10 Electrochemical performances of the PCS800/S, PCS900/S, and PCS1000/S cathodes. Cycling performances (a) and the first discharge/charge profiles (b) at 0.1 C, cycling performances at 0.5 C (c), the PCS900/S electrode with 2.5 and 4.2 mg cm^{-2} sulfur loadings (d) and long-term cycling performance at 1 C (e).

sulfur loaded electrodes is attributed to the combined effect of the large specific surface, heteroatom (N, P) doping, and stronger chemisorption trapping polysulfides of the PCS900/S material. The element-doped porous carbon sheets have good electrochemical performance and a large specific surface area, opening the door for the creation of heteroatom-doped carbon heterostructures. This shows that, in comparison with the existing lithium-ion batteries, the PCS900/S electrode may function well at high sulfur loading and is a viable material for high energy/power density Li–S batteries.

4. Conclusions

In summary, a simple pyrolysis technique has effectively produced porous carbon sheets (PCSs) that are dual doped with nitrogen and phosphorus. The intrinsic porosity of PCS900 in its as-prepared state creates a framework for the efficient adsorption of the soluble polysulfide intermediates. PCS900 is made up of micropores and mesopores. High sulfur impregnation is made possible by the abundant pore structure, which also allows for multi-channel ion transfer for polysulfides. Moreover, theoretical studies validate that the strengthened anchoring effect of polysulfides by the phosphorus doping is accountable for the outstanding electrochemical performance. PCS900/S shows good long-term cycling over 500 cycles with a capacity fading rate of 0.079% per cycle and a high areal capacity of 3.2 mA h cm^{2} (sulfur loading of 4.2 mg cm^{2}). The *in operando* microcalorimetry characterization shows that the heat released in the charging process is greater than that in the discharging process when charging and discharging with a small current; when charging and discharging with a large

current, the heat emitted during the discharging process is more than that during the charging phase. High heat generation occurs during the discharge process of lithium–sulfur batteries while charging and discharging occur at high current rates.

Author contributions

Riguang Cheng: conceptualization, data curation, formal analysis, and writing original draft. Lixian Sun: supervision of the project and advising on the critical revision of the manuscript. Pantrangi Manasa, Mi Zhou: review & editing. Jiaxi Liu and Yanxun Guan: performing XRD and TEM measurements and participating in data analysis. Kexiang Zhang, Xiangcheng Lin: data curation and formal analysis. Dan Cai: modeling and data analysis. Federico Rosei: revising the manuscript and performing data analysis. Aleskey A. Pimerzin, Hans Jürgen Seifert, and Fen Xu: performing cycling stability measurements and data analysis. Julan Zeng, Zhong Cao, and Hongge Pan: participation in the critical revision of the manuscript.

Conflicts of interest

The authors declare no conflict of interest.

Acknowledgements

This work was financially supported by the National Natural Science Foundation of China (U20A20237, 52371218, 51871065, 52271205, 51971068 and 21864009), Science and Technology Development Project of Guilin (20210102-4 and 20210216-1). Scientific Research and Technology Development Program of Guangxi (AA19182014, AD17195073, AA17202030-1 and AB21220027), Guangxi Postdoctoral Foundation, Guangxi Bagui Scholar Foundation, Guilin Lijiang Scholar Foundation, Guangxi Collaborative Innovation Centre of Structure and Property for New Energy and Materials, Guangxi Advanced Functional Materials Foundation and Application Talents Small Highlands, Chinesisch-Deutsche Kooperationsgruppe (GZ1528), the Guangxi Natural Science Foundation (2018GXNSFAA281197), and The Basic Ability Enhancement Program for Young and Middle-aged Teachers of Guangxi (2023KY0222).

References

1 Y. Liu, W. Sun, X. Lan, R. Hu, J. Cui, J. Liu, J. Liu, Y. Zhang and M. Zhu, Adding metal carbides to suppress the crystalline $Li_{15}Si_4$ formation: a route toward cycling durable si-based anodes for lithium-ion batteries, *ACS Appl. Mater. Interfaces*, 2019, **11**, 38727–38736.

2 Z. Chen, Y. Liu, Z. Lu, R. Hu, J. Cui, H. Xu, Y. Ouyang, Y. Zhang and M. Zhu, Plasma-assisted coating of nanosized SnO_2 on $LiNi_{0.5}Co_{0.2}Mn_{0.3}O_2$ cathodes for enhanced cyclic stability of lithium-ion batteries, *J. Alloys Compd.*, 2019, **803**, 71–79.

3 G. Zhang, S. Hou, H. Zhang, W. Zeng, F. Yan, C. Li and H. Duan, High-Performance and Ultra-Stable Lithium-Ion Batteries Based on MOF-Derived ZnO@ZnO Quantum Dots/C Core–Shell Nanorod Arrays on a Carbon Cloth Anode, *Adv. Mater.*, 2015, **27**, 2400–2405.

4 S. Liu, J. Li, X. Yan, Q. Su, Y. Lu, J. Qiu, Z. Wang, X. Lin, J. Huang, R. Liu, B. Zheng, L. Chen, R. Fu and D. Wu, Superhierarchical Cobalt-Embedded Nitrogen-Doped Porous Carbon Nanosheets as Two-in-One Hosts for High-Performance Lithium-Sulfur Batteries, *Adv. Mater.*, 2018, **30**, 1706895.

5 W. D. Li, Z. J. Gong, X. J. Yan, D. Z. Wang, J. Liu, X. S. Guo, Z. H. Zhang and G. C. Li, *In Situ* Engineered ZnS-FeS Heterostructures in N-Doped Carbon Nanocages Accelerating Polysulfide Redox Kinetics for Lithium Sulfur Batteries, *J. Mater. Chem. A*, 2020, **8**, 433–442.

6 X. X. Zeng, Y. T. Xu, Y. X. Yin, X. W. Wu, J. Yue and Y. G. Guo, Recent advances in nanostructured electrode-electrolyte design for safe and next-generation electrochemical energy storage, *Mater. Today Nano*, 2019, **8**, 100057.

7 H. N. Ci, J. S. Cai, H. Ma, Z. X. Shi, G. Cui, M. L. Wang, J. Jin, N. Wei, C. Lu, W. Zhao, J. Y. Sun and Z. F. Liu, Defective VSe_2-Graphene heterostructures Enabling In Situ Electrocatalyst Evolution for Lithium-Sulfur Batteries, *ACS Nano*, 2020, **14**, 11929–11938.

8 L. Chen, W. Li, L. Z. Fan, C. W. Nan and Q. Zhang, Intercalated Electrolyte with High Transference Number for Dendrite–Free Solid–State Lithium Batteries, *Adv. Funct. Mater.*, 2019, **29**, 1901047.

9 M. Sun, X. Wang, Y. Li, Z. Zhao and J. Qiu, Integration of Desulfurization and Lithium–Sulfur Batteries Enabled by Amino–Functionalized Porous Carbon Nanofibers, *Energy Environ. Mater.*, 2022, **6**, e12349.

10 W. J. Chen, B. Q. Li, C. X. Zhao, M. Zhao, T. Q. Yuan, R. C. Sun, J. Q. Huang and Q. Zhang, Electrolyte Regulation towards Stable Lithium-Metal Anodes in Lithium-Sulfur Batteries with Sulfurized Polyacrylonitrile Cathodes, *Angew. Chem., Int. Ed.*, 2020, **59**, 10732–10745.

11 R. Wang, B. Li, L. Lai, M. Hou, J. Gao and R. Wu, 3d Urchin-Like Architectures Assembled by MnS Nanorods Encapsulated in N-Doped Carbon Tubes for Superior Lithium Storage Capability, *Chem. Eng. J.*, 2019, **355**, 752–759.

12 K. Xiao, Z. Liu, Z. Chen, X. Cao, Y. Huang, H. Deng, X. Chen, Z. X. Shen and J. Liu, Unraveling the effects of anions in Ni(x)A(y)@CC (A=O, S, P) on Li-sulfur batteries, *Mater. Today Nano*, 2021, **13**, 100106.

13 W. Zhang, F. Ma, Q. Wu, Z. Zeng, W. Zhong, S. Cheng, X. Chen and J. Xie, Dual–Functional Organotelluride Additive for Highly Efficient Sulfur Redox Kinetics and Lithium Regulation in Lithium–Sulfur Batteries, *Energy Environ. Mater.*, 2022, 1–8.

14 H. J. Peng, J. Q. Huang, X. B. Cheng and Q. Zhang, Review on High-Loading and High-Energy Lithium-Sulfur Batteries, *Adv. Energy Mater.*, 2017, **7**, 1700260.

15 J. Song, Y. Jiang, Y. Lu, M. Wang, Y. Cao, L. Fan, H. Liu and G. Gao, Effective polysulfide adsorption and catalysis by polyoxometalate contributing to high-performance Li-S batteries, *Mater. Today Nano*, 2022, **19**, 100231.

16 J.-Q. Huang, T.-Z. Zhuang, Q. Zhang, H.-J. Peng, C.-M. Chen and F. Wei, Permselective Graphene Oxide Membrane for Highly Stable and Anti-Self-Discharge Lithium–Sulfur Batteries, *ACS Nano*, 2015, **9**, 3002–3011.

17 Y. Z. Zhang, K. Sun, L. Zhan, Y. L. Wang and L. C. Ling, N-doped yolk-shell hollow carbon sphere wrapped with graphene as sulfur host for high-performance lithium-sulfur batteries, *Appl. Surf. Sci.*, 2018, **427**, 823–829.

18 J. J. Cai, Z. Y. Zhang, S. R. Yang, Y. G. Min, G. C. Yang and K. L. Zhang, Self-conversion templated fabrication of sulfur encapsulated inside the N-doped hollow carbon sphere and 3D graphene frameworks for high-performance lithium-sulfur batteries, *Electrochim. Acta*, 2019, **295**, 900–909.

19 C. Li, X. L. Sui, Z. B. Wang, Q. Wang and D. M. Gu, 3d N-Doped Graphene Nanomesh Foam for Long Cycle Life Lithium-Sulfur Battery, *Chem. Eng. J.*, 2017, **326**, 265–272.

20 H. W. Wu, Y. Huang, S. Xu, W. C. Zhang, K. Wang and M. Zong, Fabricating Three-Dimensional Hierarchical Porous N-Doped Graphene by a Tunable Assembly Method for Interlayer Assisted Lithium-Sulfur Batteries, *Chem. Eng. J.*, 2017, **327**, 855–867.

21 J. R. Li, J. Zhou, T. Wang, X. Chen, Y. X. Zhang, Q. Wan and J. Zhu, Covalent Sulfur Embedding In Inherent N,P co-Doped Biological Carbon for Ultrastable and High Rate Lithium-Sulfur Batteries, *Nanoscale*, 2020, **12**, 8991–8996.

22 D. W. Rao, H. Yang, X. Q. Shen, X. H. Yan and G. J. Qiao, Immobilisation of Sulphur on Cathodes of Lithium-Sulphur Batteries via B-Doped Atomic-Layer Carbon Materials, *Phys. Chem. Chem. Phys.*, 2019, **21**, 10895–10901.

23 Y. Li, Z. Dong and L. Jiao, Multifunctional Transition Metal–Based Phosphides in Energy–Related Electrocatalysis, *Adv. Energy Mater.*, 2019, **10**, 1902104.

24 D. Tian, X. Q. Song, Y. Qiu, X. Sun, B. Jiang, C. H. Zhao, Y. Zhang, X. Z. Xu, L. S. Fan and N. Q. Zhang, Heterogeneous Mediator Enabling Three-Dimensional Growth of Lithium Sulfide for High-Performance Lithium-Sulfur Batteries, *Energy Environ. Mater.*, 2021, **5**, 1–8.

25 A. N. Arias, J. Villarroel-Rocha, K. Sapag, M. F. Mori, G. A. Planes, A. Y. Tesio and V. Flexer, High Nitrogen Content Carbons: Morphological and Chemical Changes With Synthesis Temperature and Application in Lithium–Sulfur Batteries, *Electrochim. Acta*, 2020, **359**, 136942.

26 D. B. Babu and K. Ramesha, Melamine Assisted Liquid Exfoliation Approach for the Synthesis of Nitrogen doped Graphene-Like Carbon Nano sheets from Bio-Waste Bagasse Material and its Application towards high areal density Li-S Batteries, *Carbon*, 2019, **144**, 582–590.

27 J. Cai, C. Wu, Y. Zhu, K. Zhang and P. K. Shen, Sulfur Impregnated N, P co-Doped Hierarchical Porous Carbon as Cathode for High Performance Li-S Batteries, *J. Power Sources*, 2017, **341**, 165–174.

28 S. K. Moccelini, S. C. Fernandes and I. C. Vieira, Bean sprout peroxidase biosensor based on L-cysteine self-assembled monolayer for the determination of dopamine, *Sens. Actuators, B*, 2008, **133**, 364–369.

29 J. Zhang, Y. Shi, Y. Ding, L. Peng, W. Zhang and G. Yu, A Conductive Molecular Framework Derived Li2S/N, P-Codoped Carbon Cathode for Advanced Lithium-Sulfur Batteries, *Adv. Energy Mater.*, 2017, **7**, 1602876.

30 G. Kresse and J. Furthmuller, Efficient Iterative Schemes For Ab Initio Total-Energy Calculations Using a Plane-Wave Basis Set, *Phys. Rev. B: Condens. Matter Mater. Phys.*, 1996, **54**, 11169–11186.

31 G. Kresse and D. Joubert, From Ultrasoft Pseudopotentials to the Projector Augmented-Wave Method, *Phys. Rev. B: Condens. Matter Mater. Phys.*, 1999, **59**, 1758–1775.

32 J. P. Perdew, K. Burke and M. Ernzerhof, Generalized Gradient Approximation Made Simple, *Phys. Rev. Lett.*, 1999, **78**, 1396–1396.

33 S. Grimme, Semiempirical GGA-Type Density Functional Constructed with a Long-Range Dispersion Correction, *J. Comput. Chem.*, 2006, **27**, 1787–1799.

34 A. C. Ferrari, J. C. Meyer, V. Scardaci, C. Casiraghi, M. Lazzeri, F. Mauri, S. Piscanec, D. Jiang, K. S. Novoselov, S. Roth and A. K. Geim, Raman spectrum of graphene and graphene layers, *Phys. Rev. Lett.*, 2006, **97**, 187401.

35 Z. Sun, Z. Yan, J. Yao, E. Beitler, Y. Zhu and J. M. Tour, Growth of graphene from solid carbon sources, *Nature*, 2010, **468**, 549–552.

36 J. Liu, W. Li, L. Duan, X. Li, L. Ji, Z. Geng, K. Huang, L. Lu, L. Zhou, Z. Liu, W. Chen, L. Liu, S. Feng and Y. Zhang, A Graphene-like Oxygenated Carbon Nitride Material for Improved Cycle-Life Lithium/Sulfur Batteries, *Nano Lett.*, 2015, **15**, 5137–5142.

37 J. Zhang, Y. Cai, Q. Zhong, D. Lai and J. Yao, Porous Nitrogen-doped Carbon Derived from Silk Fibroin Protein Encapsulating Sulfur as a Superior Cathode Material for High Performance Lithium-Sulfur Batteries, *Nanoscale*, 2015, **7**, 17791–17797.

38 R. Li, Z. Wei and X. Gou, Nitrogen and Phosphorus Dual-Doped Graphene/Carbon Nanosheets as Bifunctional Electrocatalysts for Oxygen Reduction and Evolution, *ACS Catal.*, 2015, **5**, 4133–4142.

39 J. Zhang, Z. Zhao, Z. Xia and L. Dai, A Metal-Free Bifunctional Electrocatalyst for Oxygen Reduction and Oxygen Evolution Reactions, *Nat. Nanotechnol.*, 2015, **10**, 444–452.

40 N. A. Cañas, S. Wolf, N. Wagner and K. A. Friedrich, *In situ* X-ray Diffraction Studies Of Lithium–Sulfur Batteries, *J. Power Sources*, 2013, **226**, 313–319.

41 J. P. Neidhardt, D. N. Fronczek, T. Jahnke, T. Danner, B. Horstmann and W. G. Bessler, A Flexible Framework for Modeling Multiple Solid, Liquid and Gaseous Phases in Batteries and Fuel Cells, *J. Electrochem. Soc.*, 2012, **159**, A1528–A1542.

42 K. Kumaresan, Y. Mikhaylik and R. E. White, A Mathematical Model for a Lithium–Sulfur Cell, *J. Electrochem. Soc.*, 2008, **155**, A576–A582.

43 J. Conder, R. Bouchet, S. Trabesinger, C. Marino, L. Gubler and C. Villevieille, Direct Observation of Lithium Polysulfides in Lithium–Sulfur Batteries Using *Operando* X-Ray Diffraction, *Nat. Energy*, 2017, **2**, 17069.

44 S. Walus, C. Barchasz, J. F. Colin, J. F. Martin, E. Elkaim, J. C. Lepretre and F. Alloin, New Insight into The Working Mechanism of Lithium-Sulfur Batteries: *In Situ* and *Operand*o, X-Ray Diffraction Characterization, *Chem. Commun.*, 2013, **49**, 7899–79901.

45 S. Waluś, C. Barchasz, R. Bouchet, J.-C. Leprêtre, J.-F. Colin, J.-F. Martin, E. Elkaïm, C. Baehtz and F. Alloin, Lithium/sulfur batteries upon cycling: Structural modifications and species quantification by in situ and operando x-ray diffraction spectroscopy, *Adv. Energy Mater.*, 2015, **5**, 1500165.

46 Y. Yan, C. Cheng, L. Zhang, Y. Li and J. Lu, Deciphering the Reaction Mechanism of Lithium–Sulfur Batteries by In Situ/Operando Synchrotron–Based Characterization Techniques, *Adv. Energy Mater.*, 2019, **9**, 1900148.

47 S. Huang, Y. V. Lim, X. Zhang, Y. Wang, Y. Zheng, D. Kong, M. Ding, S. A. Yang and H. Y. Yang, Regulating the Polysulfide Redox Conversion By Iron Phosphide Nanocrystals for High-Rate and Ultrastable Lithium-Sulfur Battery, *Nano Energy*, 2018, **51**, 340–348.

48 V. Knap, D. I. Stroe, M. Swierczynski, R. Teodorescu and E. Schaltz, Investigation of the Self-Discharge Behavior of Lithium-Sulfur Batteries, *J. Electrochem. Soc.*, 2016, **163**, A911–A916.

49 M. Kavčič, K. Bučar, M. Petric, M. Žitnik, I. Arčon, R. Dominko and A. Vizintin, *Operando* Resonant Inelastic X-ray Scattering: An Appropriate Tool to Characterize Sulfur in Li–S Batteries, *J. Phys. Chem. C*, 2016, **120**, 24568–24576.

50 J. Seo, C. S. Kim, J. Prakash and K. Zaghib, Thermal Characterization of Li/Sulfur Cells Using Isothermal Micro-Calorimetry, *Electrochem. Commun.*, 2014, **44**, 42–44.

51 G. Tonin, G. Vaughan, R. Bouchet, F. Alloin, M. Di Michiel, L. Boutafa, J.-F. Colin and C. Barchasz, Multiscale Characterization of a Lithium/Sulfur Battery by Coupling Operando X-Ray Tomography and Spatially-Resolved Diffraction, *Sci. Rep.*, 2017, **7**, 516–523.

52 C. Heubner, M. Schneider, C. Lämmel and A. Michaelis, Local Heat Generation in a Single Stack Lithium Ion Battery Cell, *Electrochim. Acta*, 2015, **186**, 404–412.

53 D. Rao, Y. Wang, L. Zhang, S. Yao, X. Qian, X. Xi, K. Xiao, K. Deng, X. Shen and R. Lu, Mechanism of Polysulfide Immobilization on Defective Graphene Sheets with N-Substitution, *Carbon*, 2016, **110**, 207–214.

54 Q. Cheng, Z. H. Yin, S. Y. Pan, G. Z. Zhang, Z. X. Pan, X. Y. Yu, Y. P. Fang, H. S. Rao and X. H. Zhong, Enhancing Adsorption and Reaction Kinetics of Polysulfides Using CoP-Coated N-Doped Mesoporous Carbon for High-Energy-Density Lithium–Sulfur Batteries, *ACS Appl. Mater. Interfaces*, 2020, **12**, 43844–43853.

55 H. Shao, F. Ai, W. Wang, H. Zhang, A. Wang, W. Feng and Y. Huang, Crab Shell-Derived Nitrogen-Doped Micro-/Mesoporous Carbon as an Effective Separator Coating for High Energy Lithium–Sulfur Batteries, *J. Mater. Chem. A*, 2017, **5**, 19892–19900.

56 H. Li, L. Sun and G. Wang, Self-Assembly of Polyethylene Glycol-Grafted Carbon Nanotube/Sulfur Composite with Nest-like Structure for High-Performance Lithium-Sulfur Batteries, *ACS Appl. Mater. Interfaces*, 2016, **8**, 6061–6071.